PHYSICS

Programmable Bloch polaritons in graphene

Lin Xiong[1†], **Yutao Li**[1†], **Minwoo Jung**[2], **Carlos Forsythe**[1], **Shuai Zhang**[1], **Alexander S. McLeod**[1], **Yinan Dong**[1,3], **Song Liu**[4], **Frank L. Ruta**[1,3], **Casey Li**[3], **Kenji Watanabe**[5], **Takashi Taniguchi**[5], **Michael M. Fogler**[6], **James H. Edgar**[4], **Gennady Shvets**[7], **Cory R. Dean**[1], **D. N. Basov**[1]*

Efficient control of photons is enabled by hybridizing light with matter. The resulting light-matter quasi-particles can be readily programmed by manipulating either their photonic or matter constituents. Here, we hybridized infrared photons with graphene Dirac electrons to form surface plasmon polaritons (SPPs) and uncovered a previously unexplored means to control SPPs in structures with periodically modulated carrier density. In these periodic structures, common SPPs with continuous dispersion are transformed into Bloch polaritons with attendant discrete bands separated by bandgaps. We explored directional Bloch polaritons and steered their propagation by dialing the proper gate voltage. Fourier analysis of the near-field images corroborates that this on-demand nano-optics functionality is rooted in the polaritonic band structure. Our programmable polaritonic platform paves the way for the much-sought benefits of on-the-chip photonic circuits.

INTRODUCTION

Photons provide an unparalleled resource for quantum technology (*1–3*), including quantum communications (*4, 5*), sensing (*6*), and computation (*7, 8*). However, free-space photons do not directly interact with electric or magnetic fields, making it difficult to efficiently program their properties. Hybridizing photons with matter gives rise to composite light-matter quasi-particles known as polaritons and creates new pathways for programmable optical phenomena (*9–11*). For example, the hybridization of photons and excitons in semiconductors results in exciton-polaritons that are amenable to both electronic and optical means of manipulation (*12–20*). Another prominent example of coupled light-matter quasi-particles are surface plasmon polaritons (SPPs), which are hybrids of photons and free electrons in conducting surfaces (*21*). Sophisticated designs of plasmonic structures have uncovered numerous ways to program SPPs (*22–24*). In complete analogy to Bloch electrons in solids or photons in photonic crystals, the dispersion of SPPs in periodic media reveals discrete bands separated by bandgaps (*25–28*). Thus, polaritonic crystals enable new means for programming the directional motion of SPPs by electrostatic control in planar gated structures.

Graphene SPPs are deeply subdiffractional optical modes (*29, 30*) with high quality factor. Systematic efforts uncovered the inherent tunability of graphene SPP wavelengths by gate voltage (*31–38*)—a feat that is difficult to achieve using alternative plasmonic media. We devised and demonstrated an as-yet-unexplored method for steering the direction of SPP travel in a pristine graphene layer. Specifically, we created a graphene polaritonic crystal (*28*) by introducing a periodic spatial modulation of the Fermi energy (*39*). In these designer crystals, graphene SPPs with continuous dispersion are transformed into Bloch polaritons residing in discrete bands (*26, 28, 40–42*). The propagation direction of Bloch polaritons is governed by the

polaritonic bands in which they reside and can be readily controlled by gate voltage. Prior demonstrations of directional SPPs all relied on manipulating the photonic constituents of the polaritonic quasi-particles by selecting the handedness of the exciting laser beam (*22, 43–50*). We programmed Bloch polaritons by controlling their matter constituents using gate voltages.

RESULTS AND DISCUSSION

A schematic of our graphene polaritonic crystal is shown in Fig. 1A. A graphene device fully encapsulated between thin layers of hexagonal boron nitride (hBN) resides on top of a Si substrate with a thermally grown SiO$_2$ layer. The SiO$_2$ layer is patterned into a hexagonal array of pillars with lattice periodicity $a = 85$ nm (*28, 39*). An infrared laser beam at energy $\omega = 890$ cm^{-1} illuminates the entire device. Patterned gold launchers on top of the device excite Bloch polaritons propagating along the polaritonic crystal (Fig. 1A) (*51*). Our patterning techniques largely preserve the quality of the graphene devices (*39*), and we achieved a polariton damping rate of $\gamma = 12$ cm^{-1} at low temperature.

Optical phenomena in our patterned polaritonic platform can be categorized under the notion of a polaritonic crystal (*25*). Specifically, the patterned substrate introduces a nanoscale periodic variation of the dielectric constants in the immediate proximity of the graphene layer. Under the application of a back gate, the variations in the capacitive coupling is imprinted as carrier density modulation in graphene (Fig. 1A, inset). Propagating polaritons scatter and interfere in regions with varying carrier densities, leading to the formation of the polaritonic band structure and Brillouin zones (BZ) (Fig. 1, B, E, and H) (*26*). At crystal momentum away from the BZ boundary, polariton dispersion is minimally affected by the periodic modulation and largely follows the dispersion in unpatterned devices as $\omega_{SPP} \propto \sqrt{E_F k}$, where E_F is the graphene Fermi energy and k is the SPP momentum. Near the boundary of the BZ, polariton dispersion is strongly modified, which leads to the formation of a complete bandgap for laser energies between 870 and 890 cm^{-1} (Fig. 1B). At a probe laser energy of $\omega = 890$ cm^{-1}, we excite polaritons residing in the upper polaritonic band. By tuning the graphene carrier density from $\bar{n}_s = 3.6 \times 10^{12}$ cm^{-2} to $\bar{n}_s = 6.0 \times 10^{12}$ cm^{-2}, the polaritonic band structure shifts upward in energy and the polaritonic bandgap emerges at 950 cm^{-1} (Fig. 1H and

[1]Department of Physics, Columbia University, New York, NY 10027, USA. [2]Department of Physics, Cornell University, Ithaca, NY 14853, USA. [3]Department of Applied Physics and Applied Mathematics, Columbia University, New York, NY 10027, USA. [4]The Tim Taylor Department of Chemical Engineering, Kansas State University, Manhattan, KS 66506, USA. [5]National Institute for Materials Science, Tsukuba, Ibaraki 305-0047, Japan. [6]Department of Physics, University of California, San Diego, La Jolla, CA 92093, USA. [7]School of Applied and Engineering Physics, Cornell University, Ithaca, NY 14853, USA.
*Corresponding author. Email: db3056@columbia.edu
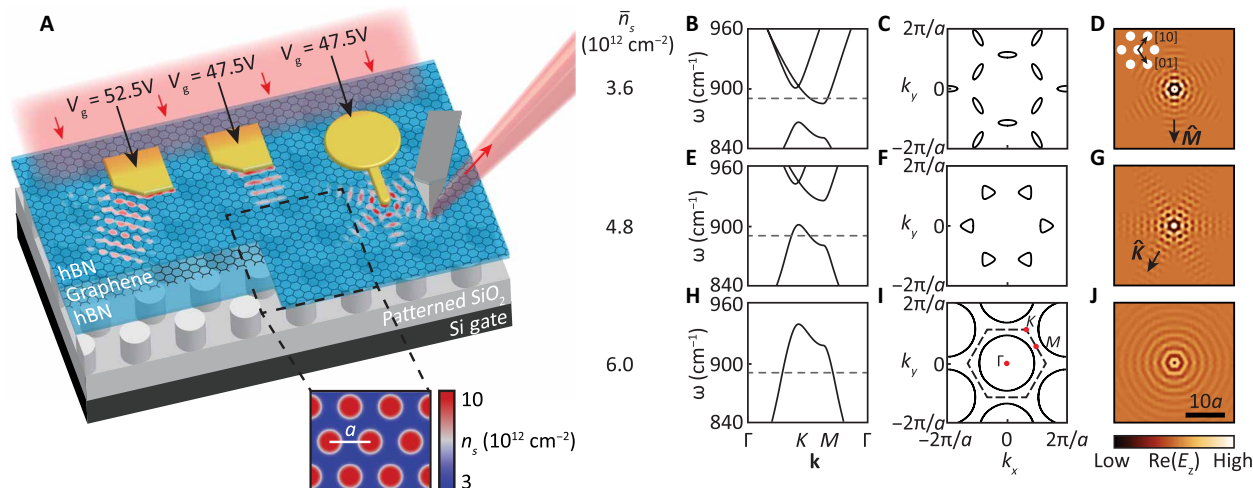†These authors contributed equally to this work.

Fig. 1. A platform for programmable Bloch polaritons. (**A**) Schematic of a back-gated graphene polaritonic crystal. Gold launchers excite Bloch polaritons propagating along designated directions controlled by the gate voltage V_g. Inset shows the carrier density distribution in the graphene layer with average carrier density $\overline{n}_s = 4.5 \times 10^{12}$ cm^{-2}. (**B**) Simulated polaritonic band structure at $\overline{n}_s = 3.6 \times 10^{12}$ cm^{-2}. Dashed line corresponds to $\omega = 890$ cm^{-1}. (**C**) Simulated equi-energy contours at $\overline{n}_s = 3.6 \times 10^{12}$ cm^{-2} and $\omega = 890$ cm^{-1}, showing the polaritonic pockets around M points. (**D**) Simulated electric field Re(E_z) of polaritons excited by a point source at $\overline{n}_s = 3.6 \times 10^{12}$ cm^{-2} and $\omega = 890$ cm^{-1}. Bloch polaritons propagate predominantly along $\widehat{M} = \langle -11 \rangle$ directions. Inset shows an enlarged real-space lattice pattern. (**E**) to (**G**), (**H**) to (**J**), same as (B) to (D) at $\overline{n}_s = 4.8 \times 10^{12}$ cm^{-2} and $\overline{n}_s = 6.0 \times 10^{12}$ cm^{-2}, respectively. At $\overline{n}_s = 4.8 \times 10^{12}$ cm^{-2}, Bloch polaritons reside in the lower band (E), emerge in the K pockets (F), and propagate along $\widehat{K} = \langle 10 \rangle$ directions (G). At $\overline{n}_s = 6.0 \times 10^{12}$ cm^{-2}, Bloch polaritons reside entirely in the lower band (H), exhibit circular equi-energy contours (I) and propagate isotropically in all directions (J). Inset of (I) shows the first BZ marked with symmetry points.

movie S1). In the latter setting, the incident laser beam excites polaritons in the lower polaritonic band. By tuning the gate voltage, we gain access to both the upper and the lower polaritonic bands (Fig. 1, B, E, and H) at a given laser energy ω.

To gain insight into the properties of Bloch polaritons, we explored the equi-energy contours (Fig. 1, C, F, and I) composed of all modes supported by the polaritonic band structure at a given laser energy ω. When ω intersects with the upper polaritonic band ($\overline{n}_s = 3.6 \times 10^{12}$ cm^{-2}, Fig. 1B) just above the bandgap, equi-energy contours emerge around M points in the BZ (Fig. 1C). The propagation direction of Bloch polaritons is governed by their group velocity, which is largely aligned with the crystal momentum in BZ. This latter conjecture is supported by real-space polariton propagation simulations where we plotted the electric field Re(E_z) of Bloch polaritons launched by a point source in the polaritonic crystal (Fig. 1D). Simulations confirm that Bloch polaritons only propagate along $\widehat{M} = \langle -11 \rangle$ directions. Provided that the laser energy falls in the polaritonic bandgap, polariton propagation is completely inhibited (not shown). Next, when the lower polaritonic band is raised further toward ω ($\overline{n}_s = 4.8 \times 10^{12}$ cm^{-2}, Fig. 1E), equi-energy contours re-emerge in the K/K' valleys (Fig. 1F). Bloch polaritons switch their propagation direction from $\widehat{M} = \langle -11 \rangle$ to $\widehat{K} = \langle 10 \rangle$ (Fig. 1G). Last, when the carrier density is increased to $\overline{n}_s = 6.0 \times 10^{12}$ cm^{-2}, the equi-energy contours evolve to near-perfect circles around the center of the BZ (Fig. 1I), and Bloch polaritons propagate isotropically in all directions (Fig. 1J), similar to their counterparts in unpatterned graphene devices. The above modeling uncovers the utility of graphene polaritonic crystals for programmable steering of Bloch polaritons.

We used low-temperature near-field optical microscopy to image Bloch polariton propagation in real space and to extract the equi-energy contours in momentum space. In these experiments, the entire device is illuminated by an infrared light from a CO_2 laser.

The metallic tip of an atomic force microscope (AFM) acts as an optical antenna that outcouples Bloch polaritons into free-space photons, enabling real-space polaritonic imaging deeply below the diffraction limit (*31*, *32*). The tip-scattered light is registered by a detector, and the amplitude $s(\mathbf{r})$ and phase $\phi(\mathbf{r})$ of the corresponding near-field signal are extracted by a proper demodulation scheme (Materials and Methods). We mainly analyzed the near-field amplitude images $s(\mathbf{r})$. All the near-field measurements were performed at $T = 60$ K to reduce SPP losses due to phonon scattering (*34*) and to minimize broadening of the polaritonic band structure.

Near-field images close to a gold launcher show directional propagation of Bloch polaritons (Fig. 2). The leading edges of the launcher form a 30° angle, thus exciting Bloch polaritons propagating along $\widehat{K}$ and $\widehat{M}$ directions (arrows in Fig. 2A). In the course of our measurements, we kept the laser energy at $\omega = 890$ cm^{-1} while tuning the gate voltage. It is instructive to plot the gate-voltage dependence of the band structure at $\omega = 890$ cm^{-1} (Fig. 2B and fig. S1). This new representation contains the same physics as Fig. 1 (B, E, and H) but facilitates a more direct connection to our imaging data. Specifically, Fig. 2B reveals that polaritons reside near M points at lower carrier densities, whereas their K point counterparts are activated at higher carrier densities. At gate voltage $V_g = 47.5$ V (Fig. 2C), Bloch polaritons only propagate along the $\widehat{M}$ direction. This phenomenon is particularly apparent when comparing the line profiles along $\widehat{M}$ (black) and $\widehat{K}$ (cyan) directions (Fig. 2F). A combination of $V_g = 47.5$ V and $\omega = 890$ cm^{-1} produces polaritonic fringes only in the $\widehat{M}$ direction, which also indicates that polaritons reside in the upper polaritonic band (Fig. 2B, top dashed line). At a slightly higher gate voltage $V_g = 52.5$ V, Bloch polariton propagation is inhibited in the $\widehat{M}$ direction, and the launcher only excites SPPs traveling diagonally along the $\widehat{K}$ direction (Fig. 2D). Line profiles in Fig. 2F confirm that Bloch polaritons propagate predominantly in the $\widehat{K}$ direction and that they can only be excited in the lower polaritonic band (Fig. 2B, middle
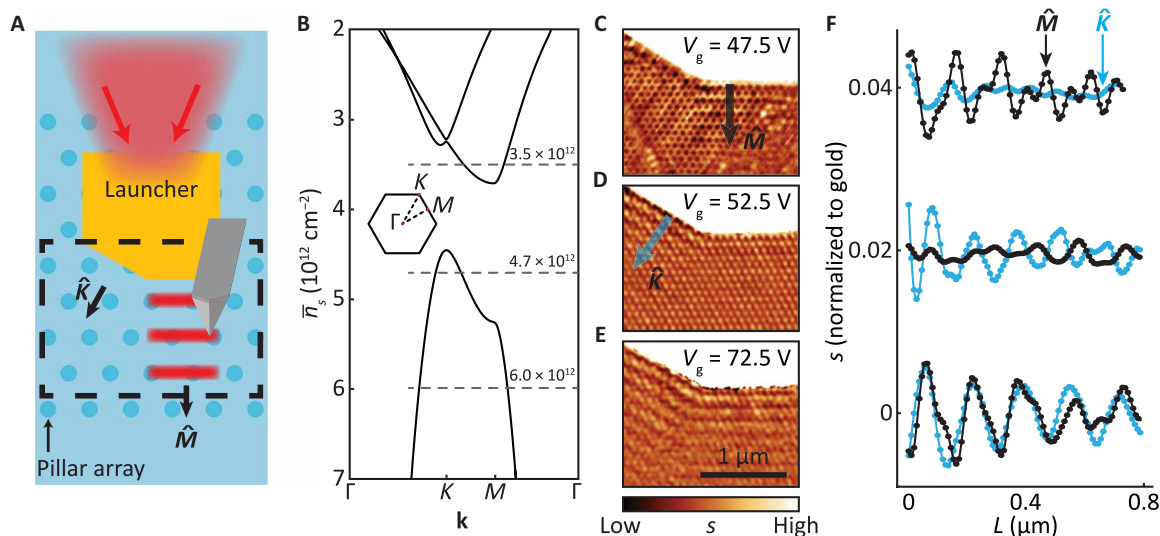
Fig. 2. Directional launching of Bloch polaritons. (**A**) Schematic of the device with the scanned region marked in the dashed box. The shades of blue colors represent different carrier densities in graphene. (**B**) Dependence of the polariton momentum **k** on average carrier density $\bar{n}_s$ at $\omega = 890$ cm^{-1}. Dashed lines correspond to the experimental conditions in (C) to (E). Inset: BZ of the polaritonic crystal marked with symmetry points. (**C**) Near-field image acquired at $T = 60$ K and $V_g = 47.5$ V. Bloch polaritons propagate in $\hat{M} = \langle -11 \rangle$ direction, as marked by the black arrow. (**D**) and (**E**) same as (C) at $V_g = 52.5$ V and $V_g = 72.5$ V, respectively. (D) shows that Bloch polaritons propagate predominantly in $\hat{K} = \langle 10 \rangle$ direction, as marked by the cyan arrow. (E) reveals isotropic polariton propagation in all directions. (**F**) Averaged line profiles along $\hat{K}$ and $\hat{M}$ directions acquired from (C) to (E). Line profiles are normalized to gold and shifted vertically by multiples of 0.02 units for clarity.
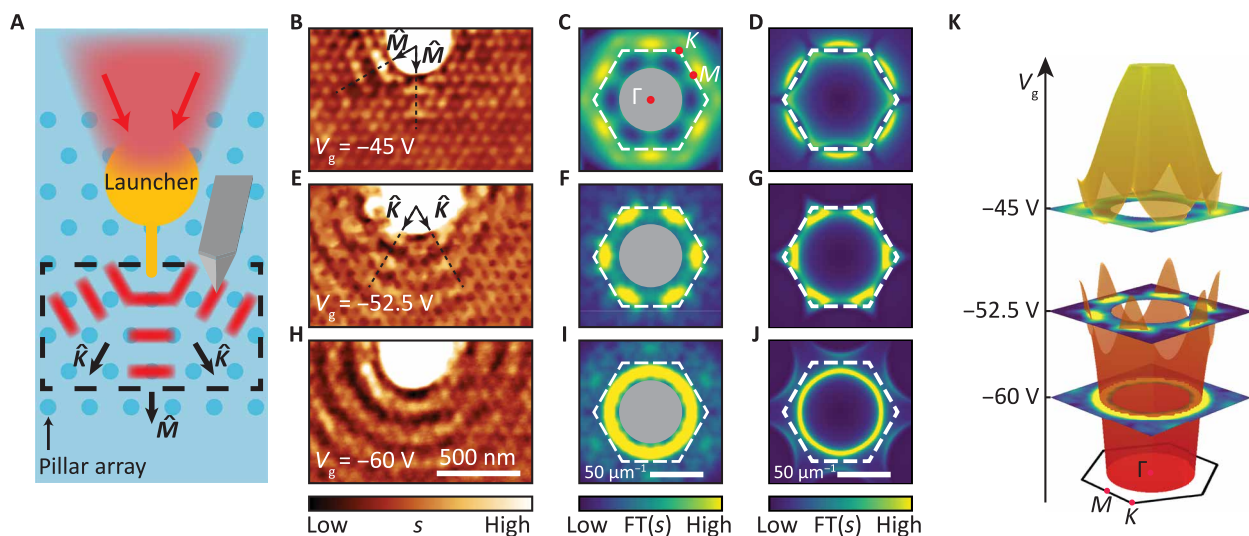

Fig. 3. Fourier analysis of polaritonic images. (**A**) Schematic of the device with the scanned region marked in the dashed box. (**B**) Near-field image obtained at $V_g = -45$ V, showing Bloch polaritons traveling predominantly in $\hat{M}$ directions. (**C**) Symmetrized Fourier transform (FT) of the image in (B). The six bright features represent Bloch polaritonic modes around M points. Polaritonic features close to the Γ point are extraneous to our study and thus are shaded in the gray circle. Inset: First BZ marked with symmetry points. (**D**) Simulated Fourier transform at $\bar{n}_s = 3.5 \times 10^{12}$ cm^{-2}. (**E**) to (**G**) same as (B) to (D) at $V_g = -52.5$ V and $\bar{n}_s = 4.8 \times 10^{12}$ cm^{-2}. Bloch polaritons propagate predominantly along $\hat{K}$ directions (E). The Fourier transform (F) shows six polaritonic pockets near K points in accord with the simulation (G). (**H**) to (**J**) same as (B) to (D) at $V_g = -60$ V and $\bar{n}_s = 6.0 \times 10^{12}$ cm^{-2}. The near-field image shows that Bloch polaritons propagate isotropically in all directions (H) and the Fourier transform (I) shows circular equi-energy contours, which agrees with the simulation (J). (**K**) Stacked equi-energy contours for selected gate voltages and overlaid with the theoretical polaritonic band structure.

dashed line). At even higher gate voltage $V_g = 72.5$ V, the laser energy is away from the polaritonic bandgap (Fig. 2B, bottom dashed line) and Bloch polaritons propagate isotropically in all directions (Fig. 2, E and F). Near-field images also reveal periodic dark spots, which are attributed to variation in the local polaritonic density of states

(28) that is peripheral to our focus on directional Bloch polaritons. We have investigated multiple devices at a variety of gate voltages across the bandgap (fig. S2). All devices show consistent control of polariton propagation by gate voltage. The agreement between our experimental observations and band structure calculations demonstrates

the ability to steer Bloch polaritons along the specified trajectories in our planar structure using the electric field effect.

Fourier analysis of the polaritonic patterns confirms that the directional launching is governed by the polaritonic band structure. Experimental inputs for this analysis are acquired by imaging Bloch polaritons emanating from the gold launcher in Fig. 3A, which resembles a point source for polaritonic waves (fig. S3). A gate voltage of $V_g = -45$ V implies that Bloch polaritons reside above the polaritonic bandgap and propagate along the $\widehat{M}$ direction (Fig. 3B). The symmetrized Fourier transform (Materials and Methods) of the near-field image (Fig. 3C) yields prominent features around M points in the BZ, forming a hexagonal motif. A similar pattern is also observed in modeling results in Fig. 3D. The agreement between gross features in the data and the modeling corroborates that the directional Bloch polariton propagation is governed by the band structure. Propagating Bloch polaritons vanish for gate voltages within the bandgap at $V_g = -50$ V (fig. S4). At even lower gate voltages such as $V_g = -52.5$ V, polariton propagation direction is switched to $\widehat{K}$ (Fig. 3E). The Fourier transform of the near-field image reveals the formation of polaritonic pockets near K points (Fig. 3, F and G, the complete field of view of the Fourier image is shown in fig. S5). Last, at $V_g = -60$ V, equi-energy contours appear as near-perfect circles within the first BZ (Fig. 3, I and J). The three selected panels of Fig. 3 (C, F, and I) are displayed again in Fig. 3K and are seen to be in close agreement with the simulated polaritonic band structure.

Outlook

We demonstrated programmable Bloch polaritons in a graphene polaritonic crystal platform. Bloch polaritons propagate along designated directions set by the applied gate voltage. The same general approach is well suited to the manipulation of other polaritonic systems, such as exciton polaritons and magnon polaritons. Relatively straightforward improvements of our platform aimed at reducing plasmonic damping and working gate voltages will enable operation at ambient conditions. Furthermore, our back-gated platform is compatible with ubiquitous metal oxide semiconductor field effect transistor technology and sets the stage for integrated photonic circuits ([52], [53]).

MATERIALS AND METHODS
Cryogenic near-field imaging techniques

Cryogenic near-field imaging measurements were performed using a home-built scattering-type scanning near-field optical microscope (s-SNOM) ([54]). The s-SNOM apparatus is based on a taping mode AFM, coupled to a continuous-wave CO_2 laser (Access Laser), operating in ultrahigh vacuum (UHV) and cryogenic temperatures. The incoming laser beam is focused on the sample using a high-NA off-axis parabolic mirror inside the UHV chamber. The metallic AFM tip is tapped above the sample surface at a frequency of ~250 kHz. The tip-scattered light is demodulated using a pseudo-heterodyne detection scheme to extract both the near-field amplitude $s(\mathbf{r}, \omega)$ and the phase $\phi(\mathbf{r}, \omega)$. The images shown in the main text are the near-field amplitude $s(\mathbf{r}, \omega)$ normalized to the gold launcher. Gold deposited using thermal evaporation serves as a good reference for the demodulated signal. To properly suppress background contributions to the near-field signal, we demodulate at the third harmonic of the tip tapping frequency ([28]).

Sample fabrication

The patterned dielectric superlattices (PDSLs) ([28], [39]) consisting of a hexagonal array of pillars were fabricated by plasma etching the SiO_2 using a thin polymethyl methacrylate (PMMA) mask. Si substrates with thermally grown SiO_2 of thickness 285 nm were spin-coated with a layer of 495 A2 PMMA of thickness 50 nm. The hexagonal pattern was written by e-beam lithography in a Nanobeam nB4 system at a current of 300 to 400 pA. SiO_2 pillars were etched in an Oxford Plasmalab 80 Plus system using a mixture of CHF_3 gas (40 sccm) and Ar gas (5 sccm) to a depth of ~50 nm. The PMMA mask was removed through an O_2 plasma etching, and the PDSL was cleaned by piranha chemical etching. The resulting superlattice is an array of pillars with 46- to 48-nm diameter and 58-nm height that form a hexagonal lattice, with lattice periodicity 85 nm in the device shown in Fig. 2 and 80 nm in the device shown in Fig. 3.

A mechanically exfoliated graphene and hBN heterostructure was placed onto the PDSL by mechanical transfer ([55]). The heterostructure consists of a top $h^{11}BN$ layer of ~4 nm, a layer of graphene, and a bottom $h^{11}BN$ layer of ~4 nm and was assembled using a polypropylene carbonate (PPC) transfer slide. Given the challenges involved in picking up an hBN layer as thin as 4 nm, such as the topmost layer, using PPC, we dug a circular hole (diameter 7 to 11 μm) out of a thick (30 to 60 nm) hBN flake using e-beam lithography. This thick hBN flake could be easily picked up by the PPC, and the thin $h^{11}BN$ and graphene flakes were positioned so that they covered the circular hole from below and could be picked up by the van der Waals interaction between them and the thick top hBN flake. Therefore, inside the circular hole (not shown in experimental images) we had a thin $h^{11}BN$-graphene-$h^{11}BN$ heterostructure. Metal contacts and launchers were deposited using standard e-beam lithography processes. The graphene device is a single crystal within our field of view, as confirmed by near-field imaging results. All the reported back gate voltages are measured from the charge neutrality point of the devices. The residual charge density in the absence of gate voltage is estimated to be $n_s = 1.75 \times 10^{11}$ cm^{-2}.

The monoisotopic $h^{11}BN$ single crystals were synthesized by the metal flux method ([56]). High-purity elemental ^{11}B (99.41%) was first mixed with Ni and Cr powders in a weight ratio of 1:12:12. These materials were then loaded into an alumina crucible and heated to a molten state with a flowing mixture of nitrogen (95%) and hydrogen (5%) at 1550°C. The $h^{11}BN$ crystals were precipitated on the flux surface by slowly cooling (1°C/hour) to 1500°C. After the growth process, the mixture temperature was quickly quenched to room temperature. The crystal flakes were obtained from the solidified flux with tape.

Symmetrization of Fourier space images

Near-field images acquired near the apex of the gold launcher were cropped to remove the gold launcher. The cropped near-field images were subsequently Fourier-transformed, using a Hann window, to get the raw image in reciprocal space. To enhance the signal-to-noise ratio and better reveal the excited polaritonic modes, we applied all the symmetry operations of the hexagonal lattice to the raw Fourier image and averaged the resulting images. More specifically, we consecutively rotated the raw Fourier image in 60° intervals, leading to six transformed images. We then applied the mirror operation to these six transformed images, resulting in six additional images. The average of all 12 transformed images results in the Fourier images shown in Fig. 3. The Fourier transform method is commonly used to analyze polaritonic equi-energy contours ([57]–[60]).

SUPPLEMENTARY MATERIALS

Supplementary material for this article is available at http://advances.sciencemag.org/cgi/content/full/7/19/eabe8087/DC1

REFERENCES AND NOTES

1. J. Wang, F. Sciarrino, A. Laing, M. G. Thompson, Integrated photonic quantum technologies. *Nat. Photonics* **14**, 273–284 (2020).
2. A. W. Elshaari, W. Pernice, K. Srinivasan, O. Benson, V. Zwiller, Hybrid integrated quantum photonic circuits. *Nat. Photonics* **14**, 285–298 (2020).
3. D. E. Chang, V. Vuletić, M. D. Lukin, Quantum nonlinear optics - Photon by photon. *Nat. Photonics* **8**, 685–694 (2014).
4. S. Slussarenko, G. J. Pryde, Photonic quantum information processing: A concise review. *Appl. Phys. Rev.* **6**, 041303 (2019).
5. F. Flamini, N. Spagnolo, F. Sciarrino, Photonic quantum information processing: A review. *Rep. Prog. Phys.* **82**, 016001 (2018).
6. S. Pirandola, B. R. Bardhan, T. Gehring, C. Weedbrook, S. Lloyd, Advances in photonic quantum sensing. *Nat. Photonics* **12**, 724–733 (2018).
7. J. Carolan, C. Harrold, C. Sparrow, E. Martín-López, N. J. Russell, J. W. Silverstone, P. J. Shadbolt, N. Matsuda, M. Oguma, M. Itoh, G. D. Marshall, M. G. Thompson, J. C. F. Matthews, T. Hashimoto, J. L. O'Brien, A. Laing, Universal linear optics. *Science* **349**, 711–716 (2015).
8. X. Qiang, X. Zhou, J. Wang, C. M. Wilkes, T. Loke, S. O'Gara, L. Kling, G. D. Marshall, R. Santagati, T. C. Ralph, J. B. Wang, J. L. O'Brien, M. G. Thompson, J. C. F. Matthews, Large-scale silicon quantum photonics implementing arbitrary two-qubit processing. *Nat. Photonics* **12**, 534–539 (2018).
9. D. N. Basov, M. M. Fogler, F. J. García De Abajo, Polaritons in van der Waals materials. *Science* **354**, aag1992 (2016).
10. D. N. Basov, A. Asenjo-garcia, P. J. Schuck, X. Zhu, A. Rubio, Polariton panorama. *Nanophotonics* **10**, 549–577 (2020).
11. D. Ballarini, S. De Liberato, Polaritonics: From microcavities to sub-wavelength confinement. *Nanophotonics* **8**, 641–654 (2019).
12. T. Chervy, P. Knüppel, H. Abbaspour, M. Lupatini, S. Fält, W. Wegscheider, M. Kroner, A. Imamolu, Accelerating polaritons with external electric and magnetic fields. *Phys. Rev. X.* **10**, 011040 (2020).
13. S. Latini, E. Ronca, U. De Giovannini, H. Hübener, A. Rubio, Cavity control of excitons in two-dimensional materials. *Nano Lett.* **19**, 3473–3479 (2019).
14. D. K. Loginov, P. A. Belov, V. G. Davydov, I. Y. Gerlovin, I. V. Ignatiev, A. V. Kavokin, Y. Masumoto, Exciton-polariton interference controlled by electric field. *Phys. Rev. Res.* **2**, 033510 (2020).
15. D. G. Suárez-Forero, F. Riminucci, V. Ardizzone, M. de Giorgi, L. Dominici, F. Todisco, G. Lerario, L. N. Pfeiffer, G. Gigli, D. Ballarini, D. Sanvitto, Electrically controlled waveguide polariton laser. *Optica* **7**, 1579–1586 (2020).
16. T. Byrnes, N. Y. Kim, Y. Yamamoto, Exciton-polariton condensates. *Nat. Phys.* **10**, 803–813 (2014).
17. R. Su, S. Ghosh, J. Wang, S. Liu, C. Diederichs, T. C. H. Liew, Q. Xiong, Observation of exciton polariton condensation in a perovskite lattice at room temperature. *Nat. Phys.* **16**, 301–306 (2020).
18. S. Klembt, T. H. Harder, O. A. Egorov, K. Winkler, R. Ge, M. A. Bandres, M. Emmerling, L. Worschech, T. C. H. Liew, M. Segev, C. Schneider, S. Höfling, Exciton-polariton topological insulator. *Nature* **562**, 552–556 (2018).
19. W. Liu, Z. Ji, Y. Wang, G. Modi, M. Hwang, B. Zheng, V. J. Sorger, A. Pan, R. Agarwal, Generation of helical topological exciton-polaritons. *Science* **370**, 600–604 (2020).
20. D. D. Solnyshkov, G. Malpuech, P. St-Jean, S. Ravets, J. Bloch, A. Amo, Microcavity polaritons for topological photonics. *Opt. Mater. Exp.* **11**, 1119–1142 (2021).
21. A. V. Zayats, I. I. Smolyaninov, A. A. Maradudin, Nano-optics of surface plasmon polaritons. *Phys. Rep.* **408**, 131–314 (2005).
22. J. Lin, J. P. B. Mueller, Q. Wang, G. Yuan, N. Antoniou, X. C. Yuan, F. Capasso, Polarization-controlled tunable directional coupling of surface plasmon polaritons. *Science* **340**, 331–334 (2013).
23. J. C. W. Song, M. S. Rudner, Chiral plasmons without magnetic field. *Proc. Natl. Acad. Sci. U.S.A.* **113**, 4658–4663 (2016).
24. D. Jin, T. Christensen, M. Soljačić, N. X. Fang, L. Lu, X. Zhang, Infrared topological plasmons in graphene. *Phys. Rev. Lett.* **118**, 245301 (2017).
25. J. J. D. Joannopoulos, S. Johnson, J. N. J. Winn, R. R. D. Meade, *Photonic Crystals: Molding the Flow of Light* (Princeton Univ. Press, 2008).
26. M. Jung, Z. Fan, G. Shvets, Midinfrared plasmonic valleytronics in metagate-tuned graphene. *Phys. Rev. Lett.* **121**, 086807 (2018).
27. S. S. Sunku, G. X. Ni, B. Y. Jiang, H. Yoo, A. Sternbach, A. S. McLeod, T. Stauber, L. Xiong, T. Taniguchi, K. Watanabe, P. Kim, M. M. Fogler, D. N. Basov, Photonic crystals for nano-light in moiré graphene superlattices. *Science* **362**, 1153–1156 (2018).
28. L. Xiong, C. Forsythe, M. Jung, A. S. McLeod, S. S. Sunku, Y. M. Shao, G. X. Ni, A. J. Sternbach, S. Liu, J. H. Edgar, E. J. Mele, M. M. Fogler, G. Shvets, C. R. Dean, D. N. Basov, Photonic crystal for graphene plasmons. *Nat. Commun.* **10**, 4780 (2019).
29. D. A. Iranzo, S. Nanot, E. J. C. Dias, I. Epstein, C. Peng, D. K. Efetov, M. B. Lundeberg, R. Parret, J. Osmond, J. Y. Hong, J. Kong, D. R. Englund, N. M. R. Peres, F. H. L. Koppens, Probing the ultimate plasmon confinement limits with a van der waals heterostructure. *Science* **295**, 291–295 (2018).
30. I. Epstein, D. Alcaraz, Z. Huang, V. V. Pusapati, J. P. Hugonin, A. Kumar, X. M. Deputy, T. Khodkov, T. G. Rappoport, N. M. R. Peres, D. R. Smith, F. H. L. Koppens, Far-field excitation of single graphene plasmon cavities with ultracompressed mode volumes. *Science* **1223**, 1219–1223 (2020).
31. J. Chen, M. Badioli, P. Alonso-González, S. Thongrattanasiri, F. Huth, J. Osmond, M. Spasenovic, A. Centeno, A. Pesquera, P. Godignon, A. Zurutuza Elorza, N. Camara, F. J. García De Abajo, R. Hillenbrand, F. H. L. Koppens, Optical nano-imaging of gate-tunable graphene plasmons. *Nature* **487**, 77–81 (2012).
32. Z. Fei, A. S. Rodin, G. O. Andreev, W. Bao, A. S. Mcleod, M. Wagner, L. M. Zhang, Z. Zhao, M. Thiemens, G. Dominguez, M. M. Fogler, A. H. Castro Neto, C. N. Lau, F. Keilmann, D. N. Basov, Gate-tuning of graphene plasmons revealed by infrared nano-imaging. *Nature* **487**, 82–85 (2012).
33. A. Woessner, M. B. Lundeberg, Y. Gao, A. Principi, P. Alonso-González, M. Carrega, K. Watanabe, T. Taniguchi, G. Vignale, M. Polini, J. Hone, R. Hillenbrand, F. H. L. Koppens, Highly confined low-loss plasmons in graphene-boron nitride heterostructures. *Nat. Mater.* **14**, 421–425 (2015).
34. G. X. Ni, A. S. McLeod, Z. Sun, L. Wang, L. Xiong, K. W. Post, S. S. Sunku, B. Y. Jiang, J. Hone, C. R. Dean, M. M. Fogler, D. N. Basov, Fundamental limits to graphene plasmonics. *Nature* **557**, 530–533 (2018).
35. A. Woessner, Y. Gao, I. Torre, M. B. Lundeberg, C. Tan, K. Watanabe, T. Taniguchi, R. Hillenbrand, J. Hone, M. Polini, F. H. L. Koppens, Electrical 2π phase control of infrared light in a 350-nm footprint using graphene plasmons. *Nat. Photonics* **11**, 421–424 (2017).
36. J. A. Gerber, S. Berweger, B. T. O'Callahan, M. B. Raschke, Phase-resolved surface plasmon interferometry of graphene. *Phys. Rev. Lett.* **113**, 055502 (2014).
37. F. C. B. Maia, B. T. O'Callahan, A. R. Cadore, I. D. Barcelos, L. C. Campos, K. Watanabe, T. Taniguchi, C. Deneke, A. Belyanin, M. B. Raschke, R. O. Freitas, Anisotropic flow control and gate modulation of hybrid phonon-polaritons. *Nano Lett.* **19**, 708–715 (2019).
38. M. B. Lundeberg, Y. Gao, R. Asgari, C. Tan, B. Van Duppen, M. Autore, P. Alonso-González, A. Woessner, K. Watanabe, T. Taniguchi, R. Hillenbrand, J. Hone, M. Polini, F. H. L. Koppens, Tuning quantum nonlocal effects in graphene plasmonics. *Science* **357**, 187–191 (2017).
39. C. Forsythe, X. Zhou, K. Watanabe, T. Taniguchi, A. Pasupathy, P. Moon, M. Koshino, P. Kim, C. R. Dean, Band structure engineering of 2D materials using patterned dielectric superlattices. *Nat. Nanotechnol.* **13**, 566–571 (2018).
40. I. Silveiro, A. Manjavacas, S. Thongrattanasiri, F. J. García De Abajo, Plasmonic energy transfer in periodically doped graphene. *New J. Phys.* **15**, 033042 (2013).
41. P. Qiu, R. Liang, W. Qiu, H. Chen, J. Ren, Z. Lin, J.-X. Wang, Q. Kan, J.-Q. Pan, Topologically protected edge states in graphene plasmonic crystals. *Opt. Express* **25**, 22587–22594 (2017).
42. M. Jung, R. G. Gladstone, G. Shvets, Nanopolaritonic second-order topological insulator based on graphene plasmons. *Adv. Photonics* **2**, 046003 (2020).
43. F. López-Tejeira, S. G. Rodrigo, L. Martín-Moreno, F. J. García-Vidal, E. Devaux, T. W. Ebbesen, J. R. Krenn, I. P. Radko, S. I. Bozhevolnyi, M. U. González, J. C. Weeber, A. Dereux, Efficient unidirectional nanoslit couplers for surface plasmons. *Nat. Phys.* **3**, 324–328 (2007).
44. Y. Liu, S. Palomba, Y. Park, T. Zentgraf, X. Yin, X. Zhang, Compact magnetic antennas for directional excitation of surface plasmons. *Nano Lett.* **12**, 4853–4858 (2012).
45. I. P. Radko, S. I. Bozhevolnyi, G. Brucoli, L. Martin-Moreno, F. J. Garcia-Vidal, A. Boltasseva, Efficient unidirectional ridge excitation of surface plasmons. *Opt. Express* **17**, 7228–7232 (2009).
46. F. J. Rodríguez-Fortuño, G. Marino, P. Ginzburg, D. O'Connor, A. Martínez, G. A. Wurtz, A. V. Zayats, Near-field interference for the unidirectional excitation of electromagnetic guided modes. *Science* **340**, 328–330 (2013).
47. N. Shitrit, I. Yulevich, E. Maguid, D. Ozeri, D. Veksler, V. Kleiner, E. Hasman, Spin-optical metamaterial route to spin-controlled photonics. *Science* **340**, 724–726 (2013).
48. L. Huang, X. Chen, B. Bai, Q. Tan, G. Jin, T. Zentgraf, S. Zhang, Helicity dependent directional surface plasmon polariton excitation using a metasurface with interfacial phase discontinuity. *Light Sci. Appl.* **2**, e70 (2013).
49. J. Petersen, J. Volz, A. Rauschenbeutel, Nanophotonics. Chiral nanophotonic waveguide interface based on spin-orbit interaction of light. *Science* **346**, 67–71 (2014).
50. S. Wang, C. Zhao, X. Li, Dynamical manipulation of surface plasmon polaritons. *Appl. Sci.* **9**, 3297 (2019).
51. P. Alonso-González, A. Y. Nikitin, F. Golmar, A. Centeno, A. Pesquera, S. Vélez, J. Chen, G. Navickaite, F. Koppens, A. Zurutuza, F. Casanova, L. E. Hueso, R. Hillenbrand,

Controlling graphene plasmons with resonant metal antennas and spatial conductivity patterns. *Science* **344**, 1369–1373 (2014).

52. T. J. Davis, D. E. Gómez, A. Roberts, Plasmonic circuits for manipulating optical information. *Nanophotonics* **6**, 543–559 (2017).

53. W. Bogaerts, D. Pérez, J. Capmany, D. A. B. Miller, J. Poon, D. Englund, F. Morichetti, A. Melloni, Programmable photonic circuits. *Nature* **586**, 207–216 (2020).

54. A. S. McLeod, E. Van Heumen, J. G. Ramirez, S. Wang, T. Saerbeck, S. Guenon, M. Goldflam, L. Anderegg, P. Kelly, A. Mueller, M. K. Liu, I. K. Schuller, D. N. Basov, Nanotextured phase coexistence in the correlated insulator V2O3. *Nat. Phys.* **13**, 80–86 (2017).

55. C. R. Dean, A. F. Young, I. Meric, C. Lee, L. Wang, S. Sorgenfrei, K. Watanabe, T. Taniguchi, P. Kim, K. L. Shepard, J. Hone, Boron nitride substrates for high-quality graphene electronics. *Nat. Nanotechnol.* **5**, 722–726 (2010).

56. S. Liu, R. He, L. Xue, J. Li, B. Liu, J. H. Edgar, Single crystal growth of millimeter-sized monoisotopic hexagonal boron nitride. *Chem. Mater.* **30**, 6222–6225 (2018).

57. P. Li, I. Dolado, F. J. Alfaro-Mozaz, F. Casanova, L. E. Hueso, S. Liu, J. H. Edgar, A. Y. Nikitin, S. Vélez, R. Hillenbrand, Infrared hyperbolic metasurface based on nanostructured van der Waals materials. *Science* **359**, 892–896 (2018).

58. W. Ma, P. Alonso-González, S. Li, A. Y. Nikitin, J. Yuan, J. Martín-Sánchez, J. Taboada-Gutiérrez, I. Amenabar, P. Li, S. Vélez, C. Tollan, Z. Dai, Y. Zhang, S. Sriram, K. Kalantar-Zadeh, S. T. Lee, R. Hillenbrand, Q. Bao, In-plane anisotropic and ultra-low-loss polaritons in a natural van der Waals crystal. *Nature* **562**, 557–562 (2018).

59. Z. Zheng, N. Xu, S. L. Oscurato, M. Tamagnone, F. Sun, Y. Jiang, Y. Ke, J. Chen, W. Huang, W. L. Wilson, A. Ambrosio, S. Deng, H. Chen, A mid-infrared biaxial hyperbolic van der Waals crystal. *Sci. Adv.* **5**, eaav8690 (2019).

60. P. Li, G. Hu, I. Dolado, M. Tymchenko, C.-W. Qiu, F. J. Alfaro-Mozaz, F. Casanova, L. E. Hueso, S. Liu, J. H. Edgar, S. Vélez, A. Alu, R. Hillenbrand, Collective near-field coupling in infrared-phononic metasurfaces for nano-light canalization. *Nat. Commun.* **11**, 3663 (2020).

61. L. Xiong, *Programmable Bloch Polaritons in Graphene* (Dryad Dataset, 2021); https://doi.org/10.5061/dryad.5mkkwh74r.